ORIGINAL

Conjugate heat transfer study comprising the effect of thermal conductivity and irreversibility in a pipe filled with metallic foams

Prakash H. Jadhav[1] · Gnanasekaran Nagarajan[1] · D. Arumuga Perumal[1]

Abstract
A parametric study is proposed in this paper to examine heat dissipation rate and entropy generation of a forced convection in a horizontal pipe which is filled with high porous metallic foams. The study quantifies the effect of thermal conductivity and pore density on entropy generation when the pipe is fully filled with copper, aluminium and nickel metallic foams of 0.6 m length in the fluid flow direction. To predict fluid flow and heat transfer features through these metallic foams the Darcy-extended Forchheimer (DEF) flow and the local thermal non-equilibrium (LTNE) models are employed. The characteristics of laminar, transition and turbulent in the non-foam region of the pipe are captured by considering the appropriate flow models. To affirm the methodology adopted in this work, the results of the present numerical solutions are validated with the available experimental results reported in the literature. Colburn j factor and thermal performance factor are the important factors that decide the performance and efficiency of any heat exchange device. Hence, these parameters are critically evaluated and are observed to increase with increasing pore densities of the metal foams and decrease with increasing flow rates of the fluid. Furthermore, the numerical analysis is extended to obtain the results of wall temperature, Nusselt number, heat transfer enhancement ratio, frictional irreversibility and Bejan number.

Nomenclature

A	Area of the pipe (m^2)
u	Velocity of fluid (m/s)
L	Length of the pipe (m)
L_f	Length of the metal foam (m)
T	Temperature (°C) or (°K)
a_{sf}	Interfacial surface area (m^{-1})
C	Form drag coefficient (m^{-1})
C_p	Specific heat of fluid (J/kg K)
d_p	Pore diameter (m)
d_f	Fiber diameter (m)
f	Friction coefficient
h	Heat transfer coefficient (W/m^2°C)
h_{sf}	Interfacial heat transfer coefficient (W/m^2°C)
K	Permeability (m^2)
Pr	Prandtl number
Re	Reynolds number based on hydraulic diameter
q"	heat flux (W/m^2)
Re_{d_f}	Reynolds number based on fiber diameter
D	Diameter of the pipe (m)
D_h	Hydraulic diameter of the pipe (m)
λ	Thermal conductivity (W/m°C)
P	Perimeter of the pipe (m)
$\overline{Nu}$	Average Nusselt number filled foam pipe
$\overline{Nu_\Phi}$	Average Nusselt number of empty pipe
Nu_{ER}	Heat transfer enhancement ratio

Greek symbols

ε	Porosity
λ	Thermal conductivity (W/m°C)
μ	Dynamic viscosity of the fluid (Ns/m^2)
ν	Kinematic viscosity (m^2/s)
ρ	Density of the fluid (kg/m^3)

Super subscript

i	Each data points/Local data points

Subscript

ER	Enhancement ratio
w	Wall
f	Fluid
eff	Effective

✉ Gnanasekaran Nagarajan
gnanasekaran@nitk.edu.in

Prakash H. Jadhav
jdvprakash@gmail.com

D. Arumuga Perumal
perumal@nitk.edu.in

[1] Department of Mechanical Engineering, National Institute of Technology Karnataka, Surathkal 575025, India

s   Solid
se   Solid effective
fe   Fluid effective

1 Introduction

The performance of thermal engineering system has been affected by thermal irreversibility losses which lead to rise of entropy generation and loss in thermal efficiency of the system. Metal foams are widely used for engineering applications in cooling of heat exchangers, solar collectors, electronic cooling etc.

Nazari et al. [1] conducted experiments on convection heat dissipation using nano-fluid in a circular pipe filled with metallic foam. It is observed that there was considerable advancement in the heat dissipation at the cost of pressure loss with the use of Al_2O_3 nano-fluid. Xu et al. [2, 3] suggested that the hallow ratio less than 0.3 gives higher thermal performance factor. The heat transfer enhancement is more advanced in local thermal equilibrium (LTE) model compared to LTNE model because convective thermal resistance is low. The porous metal foam conductivity and porosity play a significant role in the calculation of heat dissipation rate with LTNE model.

In comparison with average Nusselt number, the LTE and LTNE models confirm similar results when the velocity of air is high. Since, the LTE model used to envisage thermal performance of metal foam at high velocity flow and has large height, the state of thermal equilibrium is achieved as reported by Lin et al. [4]. Lu et al. [5] explored analytical investigation on fluid and heat flow features of a fixed parallel plate partly filled with metallic foam. The temperature and velocity outlines are predicted for various pore densities of the metallic foam.

Under mixed convection, the interfacial convection heat transfer coefficient increases when Reynolds number exceeds 100 and Richardson (Ri) number varies from 0.01 to 10 reported by Celik et al. [6]. In the variation of thickness of copper and aluminum foams, the copper metallic foam enhance only 4 percentage upsurge in heat dissipation rate than aluminum metallic foam. [7]. Gangapatnam et al. [8] observed that the LTE model under predicts the heat dissipation while the LTNE model gives accurate results of heat dissipation in terms of Nusselt number. Li et al. [9] the LTNE with Monte Carlo method was employed to calculate the radiation heat emission rate. It has been reported that the pore density of 15 with porosity 0.95 greatly involves in obtaining 20% radiation heat flux from the entire wall heat flux.

Baragh et al. [10] performed forced convection analysis in a single-phase flow through circular pipe with different arrangement of porous medium. They considered six different arrangement of porous medium for various flow regimes like laminar, transition and turbulent inside the channel. They recorded that with increasing size of porous medium, thermal performance increases with respect to Reynolds number. When the diameter of the porous medium is equal to the diameter of the pipe, it is found that the rate of heat dissipation as well as enhancement ratio is higher compared to other configurations considered in the study of laminar and turbulent flows.

The porous media show a vital role in the enhancement of heat dissipation rate; convective coefficient increases by 2.2 times the base line as reported by Sheikhnejad et al. [11]. It is reported that at higher frequencies, 20 PPI metal foam develops maximum inlet pressure compared to 10 PPI and 40 PPI metal foams and at lower frequencies 10 PPI metal foam yields maximum inlet pressure related to 20 PPI and 40 PPI foams as presented by Bagci and Dukhan [12]. Abadi and Kim [13] proposed a correlation to determine convective coefficient and pressure drop for small tube filled with metallic foam.

The addition of 75% metal foam filling in the tube shows better results for 40 PPI as that of 50% filling rate of 20 and 10 PPI metallic foams. The importance of LTE and LTNE models for forced convection in a conduit occupied with porous medium is detailed in [14–16]. Based on the exact solutions, the LTNE model clearly shows that the LTE model may fail for the combination of air and metallic foam. Lu and Zhao [17] reported various flow regimes from the $\Delta P/LV$ - Reynolds number results. They noticed that with increasing porosity of the porous medium the convection heat transfer increases rather than conduction heat transfer.

Magyari and Storesletten [18] observed that with horizontal and inclined porous channel (i.e., inclination angle less than 90°), the boundary value problem states unique and multiple solutions for known values of Ra and dimensionless velocity. Alomar [19] two-phase flow model is established since non-Darcy flow model and LTNE model circumstances to define the problem for complete evaporation. Tio et al. [20] the results explored that, the buoyancy has the effect on performance of heat pipe with respect to angle of inclination. Suggested new generalized approach for modelling to adopt effective thermal conductivity and pore scale analysis are explained in detailed [21, 22]. Examined experimentally and numerically the forced convection heat dissipation through the porous medium using 20 screen wire mesh. Also, they reported that among Darcy-LTE and LTNE, Brinkman-LTE and LTNE, the Brinkman-LTNE model gives better results which is detailed in [23, 24].

To determine thermal irreversibility on account of heat and fluid friction in a thermal system, the idea of entropy generation rate analysis was presented by Bejan [25]. To augment efficiency of the thermal system, the entropy generation has to be minimized [26–28]. Modeling of saturated porous media is done by employing Brinkman flow model to capture behavior of fluid

flow in forced convection [29, 30]. Additionally, the average exergy transfer Nusselt number (Nu_e) declines with increasing Reynolds number. The drying rate is slightly more in case of fine particle bed compared to coarse particle bed and this is due to higher capillary pressure action reported in [31, 32].

When flow through pores takes place, mechanical energy is dissipated as heat which results in viscous dissipation. This pore level effect can be accounted by macroscopic study which deals with viscous dissipation in thermal energy equation. It is well known that the available work of a system is destroyed by entropy generation. For an efficient design of a thermal system, it is important to focus the generation of entropy due to fluid flow and heat transfer processes. Further, the irreversibility associated with the thermal system can alter the efficiency and it is desirable to minimize such entropy generation. Torabi et al. [33, 34] observed that with the increment in Peclet number the local entropy generation rate increases. Furthermore, the nanoparticles concentration has negligible effect on temperature inside the porous insert. Variation in concentration of nanoparticles has significantly affected local and total entropy generation. Furthermore, the total entropy generation advanced monotonically with increment in thermal conductivity ratio and the wall thickness. They noticed that the entropy generation advance with decrease in aspect ratio. Nevertheless, for Bejan number (Be) less than 0.5, the fluid frictional irreversibility influence over the thermal irreversibility. However, the Bejan number is found to be minimum at the center of pipe and increases to a maximum towards wall of the pipe [35–38].

Bekir and Yilbas [39] with increasing inlet port height of the channel the entropy generation increases gradually because of heat dissipation for inlet port of the height beyond 0.03 m. Nonetheless entropy generation drops with increasing porosity of the porous block. Tayari et al. [40] they recorded that the total entropy generation is obtained least for the angles 0° and 180, and it advanced at an angle close to 70°. Nazari et al. [41] they found that for fixed diameter of sphere with heat generation, the Nu_e reduces with increment in Re and also it reaches towards zero for the Reynold's number 1450, 1800 and 2300 respectively. The surface Nusselt number and entropy production rate increase with an increase in flow rates as well as with increase in angle among the pitches of AEA tube [42–44].

It is clear from the aforementioned literature that the metallic foams are being utilized to enhance heat transfer in heat exchanging devices. Researchers have highlighted the entropy generation during forced convection and mixed convection heat dissipation in horizontal/inclined pipe which is filled partially or fully with porous medium. Though rich literature is available in this research, modeling entropy generation in porous media is still harder than the clear fluid phenomena and choosing appropriate models for viscous dissipation to understand the physics is quite challenging. Researchers are looking for alternative foams against the conventional copper foams.

Therefore, in this work, the entropy generation rate is not only effectively analyzed with respect to the pore density and porosity but also with different materials of metallic foams. Moreover, the analysis is performed for a wide range of Reynolds number varied from 1125 to 8500 that gives a comprehensive information on different flow regimes along with the PPI, porosity and various metal foams. The present study also provides an important comparison study between the use of various metallic foams and wire mesh reported by Baragh et al. [10]. Further, the study proposed in the work helps extend more parametric studies such as optimizing the size of the foam, thermal conductivity of the foam, discrete foams, different heating length, minimizing pressure drop etc.

2 Geometry

The present investigation considers a cylindrical pipe of 0.1 m diameter and a thickness of 7 mm made up of aluminum material. The problem domain is analogous to the experimental setup considered by Baragh et al. [10]. The pipe wall is attached with heater around the circumference and the heater is assigned with constant heat input. Aluminum, copper and nickel metal foams of various pore densities with different porosities are filled in the pipe to improve the thermal performance which leads to minimizing the entropy production rate for designing an effective thermal system. The metal foam is having dimension of 0.1 m diameter and a length of 0.6 m and is placed exactly at the center of the pipe. In the present analysis, the metallic foam pore densities of 10, 20, 30 and 40 with porosities varying from 0.85 to 0.95 are considered as per Lu et al. [5]. The schematic of the pipe along with the metallic foam filling is represented in Fig. 1. The thermal performance and entropy generation through the pipe are determined for Reynolds number ranging from 1125 to 8500.

3 Numerical domain with details of boundary conditions

The pipe is symmetry at the centerline along the z-direction of flow [45]; hence, a 2-D computational domain is considered for further numerical computations and is shown in Fig. 2. The upstream domain is extended by 2 L in order to accomplish a developed flow before fluid enters to the test section [46]. Similarly, the downstream of the domain is extended by 1.5 L in order get one way coordinate and to avoid the exit effects [4]. A uniform velocity profile is applied at the inlet while zero pressure is defined at the outlet. The upstream and downstream walls of the pipe are assigned with adiabatic wall conditions. The heater is coupled to pipe wall and is defined with uniform heat flux while the axis of the pipe is defined with axis symmetry boundary condition. At the interior

Fig. 1 Illustration of the circular pipe
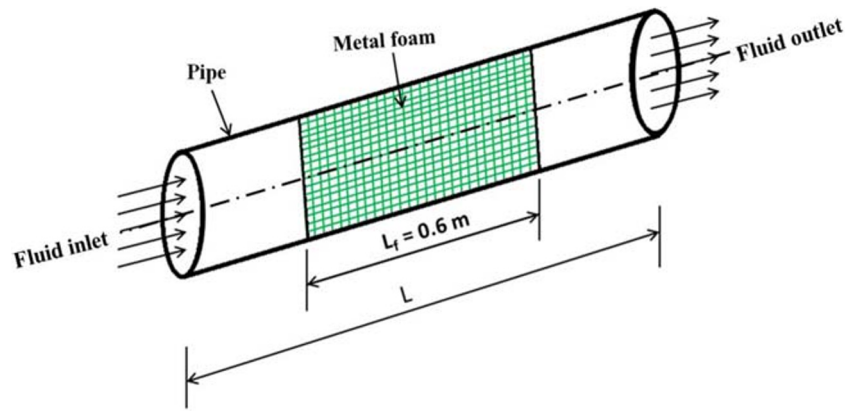
surface amongst the foam and foam free region, the continuous in shear stress and energy is incorporated as stated by several investigators [7].

Due to axis symmetry, only upper half of the pipe is considered for computational domain [47]. At r = 0, symmetry at centerline causes the velocity gradients and temperature gradients to be zero in r direction. At entry of the fluid, Z = 0, $v =$ 0, T = T_{in}, u = u_{in} and at the exit of the pipe Z = 4.5 L, the gradients of u, v and T along Z – direction are zero. Details of boundary conditions used for the computational domain are presented in Table 1 [47].

4 Details of numerical simulation

The numerical simulations are performed with commercially existing software ANSYS FLUENT 15.0 (ANSYS, 2017). A conjugate heat dissipation study is accomplished for the computational domian as it consists of solid aluminium pipe wall and fluid flowing through clear and porous regions of the pipe. The fluid considered is air and the properties are calculated at inlet temperature. The velocity of the fluid varies from 0.17 m/s to 1.25 m/s; hence, the Re is evaluated based on D_h of pipe ranging between 1125 and 8500. Based on the Re, the flow is assumed to be laminar, transition and turbulent. The k-kl-ω model is used for predicting transition flow features and k-ε model is adopted to capture the features of turbulent flow in the non-porous region of the pipe [4, 48–50].

The governing equations employed to compute non-foam region of fluid flow through the pipe are as follows [47, 51].

Continuity equation:

$$\frac{\partial}{\partial z}(\rho u) + \frac{1}{r}\frac{\partial}{\partial r}(r\rho v) = 0 \tag{1}$$

Z – momentum equation in clear region:

$$\frac{\partial}{\partial z}(\rho uu) + \frac{1}{r}\frac{\partial}{\partial r}(r\rho vu) = -\frac{\partial p}{\partial z} + \frac{\partial}{\partial z}\left(\mu_f \frac{\partial u}{\partial z}\right) + \frac{1}{r}\frac{\partial}{\partial r}\left(r\mu_f \frac{\partial u}{\partial r}\right) \tag{2}$$
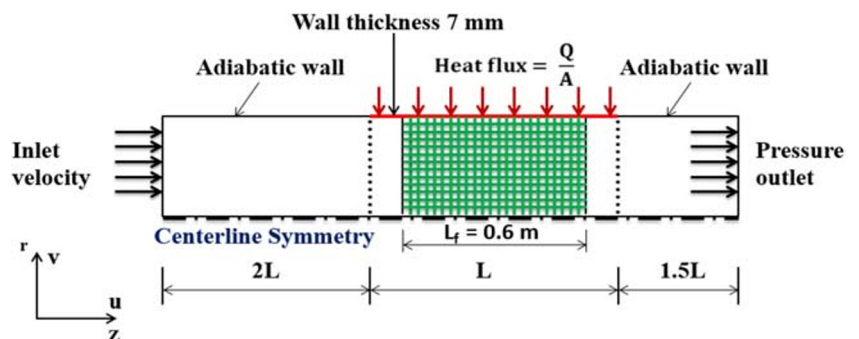
r – momentum equation in clear region:

$$\frac{\partial}{\partial z}(\rho uv) + \frac{1}{r}\frac{\partial}{\partial r}(r\rho vv) = -\frac{\partial p}{\partial r} + \frac{\partial}{\partial z}\left(\mu_f \frac{\partial v}{\partial z}\right) + \frac{1}{r}\frac{\partial}{\partial r}\left(r\mu_f \frac{\partial v}{\partial r}\right) - \frac{\mu_f v}{r^2} \tag{3}$$

Energy equation in clear region:

$$\frac{\partial}{\partial z}(\rho C_p uT) + \frac{1}{r}\frac{\partial}{\partial r}(\rho C_p rvT) = \frac{\partial}{\partial z}\left(\lambda_f \frac{\partial T}{\partial z}\right) + \frac{1}{r}\frac{\partial}{\partial r}\left(r\lambda_f \frac{\partial T}{\partial r}\right) \tag{4}$$

Fig. 2 Illustration of numerical domain

Table 1 Boundary conditions used for computational domain

Boundaries		Boundary conditions
Inlet	Uniform velocity	$Z = 0$, $u = u_{in}$, $v = 0$, $T = T_{in}$
Outlet	Zero pressure	$Z = 4.5$ L, $\frac{\partial u}{\partial r} = 0$, $\frac{\partial v}{\partial Z} = 0$, $\frac{\partial T}{\partial Z} = 0$
Entry wall and exit wall	Adiabatic	$r = R$, $v = 0$, $u = 0$, $\frac{\partial T}{\partial r} = 0$
Heated wall	Uniform heat flux	$r = R$, $u = 0$, $v = 0$, $q = q"$
Horizontal axis	Symmetry	$r = 0$, $v = 0$, $\frac{\partial u}{\partial r} = 0$, $\frac{\partial T}{\partial r} = 0$

The details regarding the governing equations of k-kl-ω transition and k-ε (k-epsilon) turbulent models are listed in [4, 48–50]. The porous metallic foam is taken as isotropic homogeneous medium and modeled using DEF flow model in the current computational domain. The DEF model is added to the momentum equation as a source term; the inertial and viscous loss terms are considered because of permeability and form drag coefficient, respectively of the porous medium. The governing equations adopted for computing the porous medium are as follows [47, 51].

Z – momentum equation in porous region:

$$\frac{1}{\varepsilon^2}\frac{\partial}{\partial z}(\rho u u) + \frac{1}{r\varepsilon^2}\frac{\partial}{\partial r}(r\rho v u) = -\frac{\partial p}{\partial z} + \frac{1}{\varepsilon}\frac{\partial}{\partial z}\left(\mu_{eff}\frac{\partial u}{\partial z}\right) + \frac{1}{r\varepsilon}\frac{\partial}{\partial r}\left(r\mu_{eff}\frac{\partial u}{\partial r}\right) - \frac{\mu_{eff}u}{K} - \frac{\rho F}{\sqrt{K}}|u|u \tag{5}$$

r – momentum equation in porous region:

$$\frac{1}{\varepsilon^2}\frac{\partial}{\partial z}(\rho u v) + \frac{1}{r\varepsilon^2}\frac{\partial}{\partial r}(r\rho v v) = -\frac{\partial p}{\partial r} + \frac{1}{\varepsilon}\frac{\partial}{\partial z}\left(\mu_{eff}\frac{\partial v}{\partial z}\right) + \frac{1}{r\varepsilon}\frac{\partial}{\partial r}\left(r\mu_{eff}\frac{\partial v}{\partial r}\right) - \frac{\mu_{eff}v}{K} - \frac{\rho F}{\sqrt{K}}|u|v - \frac{\mu_{eff}v}{\varepsilon r^2} \tag{6}$$

Energy equation: LTNE

i. for fluid phase:

$$\frac{\partial}{\partial z}(\rho C_p u T) + \frac{1}{r}\frac{\partial}{\partial r}(\rho C_p r v T)$$
$$= \frac{\partial}{\partial z}\left(\lambda_{fe}\frac{\partial T}{\partial z}\right) + \frac{1}{r}\frac{\partial}{\partial r}\left(r\lambda_{fe}\frac{\partial T}{\partial r}\right) + h_{sf}a_{sf}(T_s - T_f) \tag{7}$$

ii. for solid phase

$$0 = \frac{\partial}{\partial z}\left(\lambda_{se}\frac{\partial T}{\partial z}\right) + \frac{1}{r}\frac{\partial}{\partial r}\left(r\lambda_{se}\frac{\partial T}{\partial r}\right) - h_{sf}a_{sf}(T_s - T_f) \tag{8}$$

where,

$$\lambda_{se} = (1-\varepsilon)\lambda_{fe} \text{ and } \lambda_{fe} = \varepsilon \lambda_f \tag{9}$$

where, λ_{se} and λ_{fe} represents the effective thermal conductivity of solids and fluid respectively, λ_f represents the thermal conductivity of fluid, μ_{eff} represents effective viscosity which is equivalent to the viscosity of operating fluid, K denotes the permeability, ε is the porosity of the metal foam and F represents form drag coefficient or inertia parameter.

It is mandatory to report that the heat dispersion in the metallic foam is treated to be insignificant in the current numerical computation owing to high thermal conductivity metallic foam and working fluid air [Calmidi and Mahajan [52]]. Similarly, the blending of fluid flow due to circuitous passage of the motion inside the metallic foam is neglected in the current numerical investigation. The solution method includes pressure-velocity coupling through pseudo transient explicit relaxation scheme. The spatial discretization of second order is considered for momentum, pressure, turbulent dissipation rate, turbulent kinetic energy and energy equation. The convergence criteria for continuity and momentum equation is fixed as 10^{-5}, for k-kl-ω and k-ε is fixed as 10^{-3} and for energy equation is fixed as 10^{-8}.

In the current work the metal foam properties such as superficial area density (a_{sf}) and interfacial heat transfer

coefficient (h_{sf}) are evaluated based on Eqs. (10) and (11), respectively as suggested [52, 53].

Superficial area density,

$$a_{sf} = \frac{3\pi d_f \left(1 - exp^{-\left(\frac{1-\varepsilon}{0.04}\right)}\right)}{\left(0.59 d_p\right)^2} \qquad (10)$$

Interfacial heat transfer coefficient,

$$\frac{h_{sf} d_f \left(1 - exp^{-\left(\frac{1-\varepsilon}{0.04}\right)}\right)}{\lambda_f} = \begin{cases} 0.76 \, Re_{d_f}{}^{0.4} \, Pr^{0.37}, \left(1 \leq Re_{d_f} \leq 40\right) \\ 0.52 \, Re_{d_f}{}^{0.5} \, Pr^{0.37}, \left(40 \leq Re_{d_f} \leq 10^3\right) \\ 0.26 \, Re_{d_f}{}^{0.6} \, Pr^{0.37}, \left(10^3 \leq Re_{d_f} \leq 2 \times 10^5\right) \end{cases} \qquad (11)$$

where α_f is the thermal conductivity of operating fluid, Pr represents Prandtl number, Re_{d_f} represents Reynolds number which is evaluated based on the fiber diameter of the porous, refer Eq. (12).

$$Re_{d_f} = \left\{ u d_f \left(\frac{1 - exp^{-\left(\frac{(1-\varepsilon)}{0.04}\right)}}{\varepsilon \nu}\right) \right\} \qquad (12)$$

where, d_f represents the fiber diameter in m and d_p represents the pore diameter.

The properties of metallic foam such as pore size, fiber diameter, permeability and inertial coefficient are calculated using Table 2 as per Lu et al. [5].

5 Second law analysis

To evaluate the total irreversibility developed in the presence of metal foam inside the horizontal pipe due to heat dissipation and fluid friction, the thermal entropy generation is computed using the Eq. (13) and given as [54].

$$S\cdot_{g,HT} = \frac{q''^2 \pi D_h{}^2 L}{\lambda_{eff} T_{f,in} T_{f,out} \overline{Nu}} \qquad (13)$$

where, $S\cdot_{g,HT}$ denotes thermal entropy generation, q'' denotes continuous heat input W/m^2, λ_{eff} represents effective conductivity of the metallic foam in (W/mK), $T_{f,in}$ denotes fluid inlet temperature (K), $T_{f,out}$ represents fluid outlet temperature (K), $\overline{Nu}$ is the average Nusselt number.

The frictional entropy generation is computed as [54].

$$S\cdot_{g,FF} = \frac{8 m\cdot^3 L f}{\pi^2 \rho^2 \left(\left(T_{f,in} + T_{f,out}\right)/2\right) D_h{}^5} \qquad (14)$$

where, $S\cdot_{g,FF}$ is the fluid frictional entropy generation, $m\cdot$ denotes mass flow rate of fluid (kg/s), L denotes length of pipe (m), f denotes friction factor, ρ denotes fluid density (kg/m^3). The total entropy generation rate is associated with fluid friction and heat transfer is given in Eq. (15).

Total entropy generation rate, $\quad S\cdot_{g,T} = S\cdot_{g,HT} + S\cdot_{g,FF}$ (15)

To study the contribution of thermal entropy, frictional entropy and total entropy generation rate, a dimensionless parameter called Bejan number (Be) and is defined as the ratio of thermal entropy generation rate to the total entropy generation rate. Obviously, the value of the Bejan number ranges from 0 to 1 [55].

$$Be = \frac{S\cdot_{g,HT}}{S\cdot_{g,HT} + S\cdot_{g,FF}} \qquad (16)$$

6 Grid independence study

The grid sensitivity analysis is performed to obtain an optimal grid size. To perform this, 10PPI aluminium metallic foam with porosity of 0.85 is considered for the Re of 1700 and continuous heat flux of 275 W/m^2 for the heater. The investigation is performed on five distinct grid sizes: 42701, 47,751, 67,281, 86,811 and 106,341. The deviation of wall temperature and pressure drop for four distinct grid sizes is evaluated and reported in Table 3. Amongst five different grid sizes, the

Table 2 Correlation used to compute the properties of metallic foam

S. \No.	Properties	Correlations
1	Pore size (d_p)	$d_p = \frac{0.0254}{PPI}$
2	Fiber diameter (d_f)	$\frac{d_f}{d_p} = 1.18 \sqrt{\frac{(1-\varepsilon)}{3\pi}} \left(\frac{1}{1 - e^{\left(\frac{(1-\varepsilon)}{0.04}\right)}}\right)$
3	Permeability (K)	$K = 0.00073 \, (1-\varepsilon)^{-0.224} \left(\frac{d_f}{d_p}\right)^{-1.11} d_p^2$
4	Inertial/Form coefficient (CI)	$CI = 0.00212 (1-\varepsilon)^{-0.132} \left(\frac{d_f}{d_p}\right)^{-1.63}$

Table 3 Grid independence analysis

Grid sizes	T_w (°C)	ΔP (Pa)	Deviation (%)	
			T_w	ΔP
42,701	48.48	49.48	6.04	2.2
47,751	47.42	50.48	3.72	0.26
67,281	46.24	50.53	1.14	0.079
86,811	45.89	50.56	0.37	0.02
106,341	45.72	50.57	Base line	

grid size of 86,811 is seen to have less error; hence, the same is chosen for further computations.

6.1 Validation of numerical results

The numerical results of the wall temperature at the top surface is validated with experimental results of Garrity et al. [56] for the pore densities of 10, 20 and 40 PPI aluminium metallic foam and is given in Fig. 3. From Fig. 3 it is observed that there is relatively larger deviation amongst numerical computational results and experimental results at low mean velocity of fluid for all three PPI of aluminium metallic foam. However, the deviation gradually reduces and matches well with higher mean velocities of the fluid flow. The results found in current investigation are agreeing with the results found by [4, 7].

The methodology in the current investigation is validated by matching numerical data of pressure drop for 40 PPI aluminium metal foam with experimental data of Garrity et al.

[56], refer Fig. 4. Figure 4 explored that the predicted results of pressure drop obtained by the numerical simulation is in better agreement with experimental data of Garrity et al. [56]. The deviation of pressure drop gradually increases at higher flow rates of fluid. However, the average deviation in pressure drop is found to be 7.04%.

To adopt the solution methodology, the numerical simulation is performed by considering similar analytical model and similar parameters used in Lu et al. [5]. Figure 5 represents the comparison of velocity profile for fully filled aluminum metallic foam between the present numerical results and the analytical results of Lu et al. [5]. From the figure, it is clear that the dimensionless velocity profile obtained from the numerical studies is well coinciding with the analytical results of Lu et al. [5]. This also serves as a validation of the present methodology.

Further, to adopt the computational methodology for the pipe filled with aluminium metallic foam, the wall temperature obtained along the length of the pipe is compared with experimental data of Baragh et al. [10] and is depicted in Fig. 6. In the numerical computation, the aluminium metal foam of 30 PPI with different porosities is compared with the experimental data reported by Baragh et al. [10]. The uniform heat flux is assigned over entire 1 m length of the pipe and the metallic foam is attached exactly at the center of the pipe along the flow direction i.e., 0.2 L to 0.8 L. As the fluid enters the test section (i.e., non-foam region of the pipe 0 to 0.2 L) the heat is transferred instantly to the fluid due to the temperature difference between the flowing fluid and heated wall by means of convection heat transfer. Also, the wall
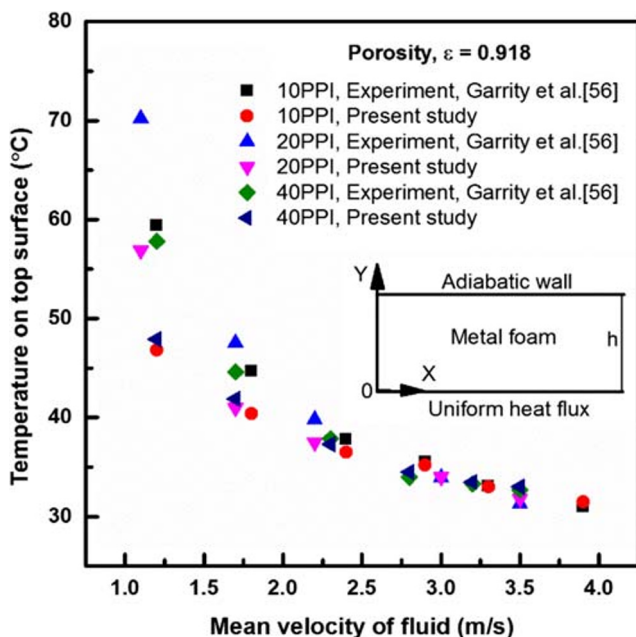
Fig. 3 Variation of temperature on the top surface ($x = 0.5\ l$) of aluminium metallic foam
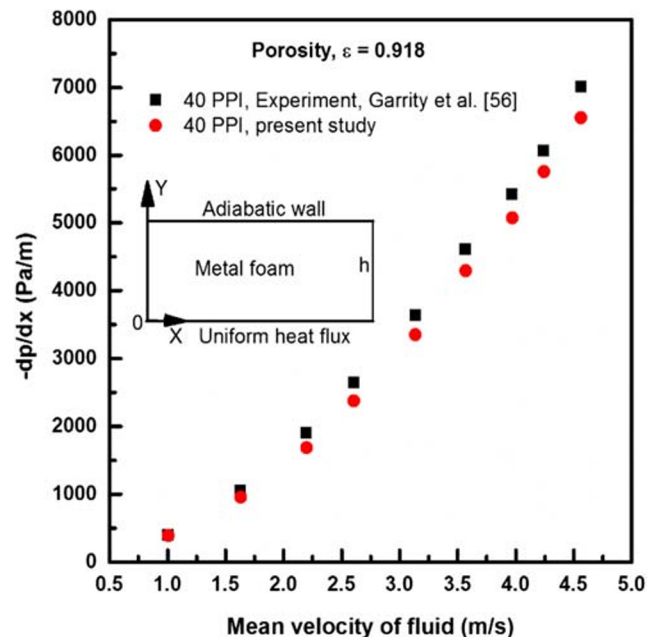
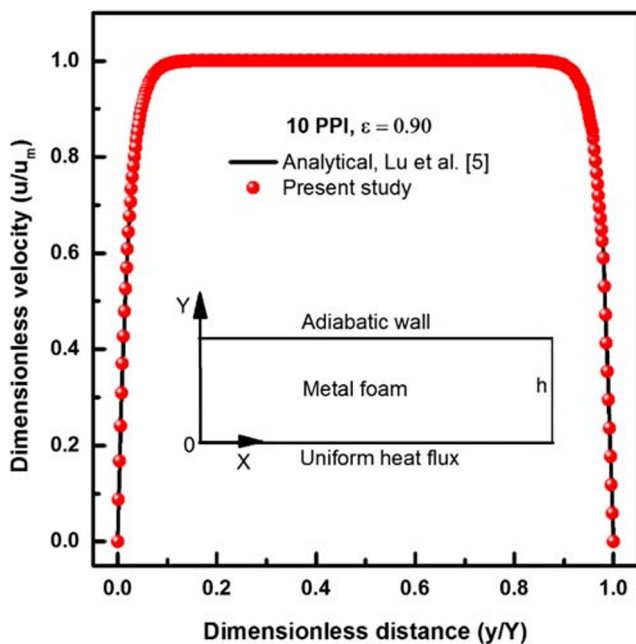**Fig. 4** Variation of pressure drop through aluminium metal foam ($l = 0.1524$ m) with mean velocity of fluid

Fig. 5 Velocity profile for fully filled aluminium metal foam

Fig. 6 Wall temperature of the current study compared with experimental results of Baragh et al. [10]

temperature at the entry region of pipe (i.e., 0 to 0.2 L) is lower compared to the exit region (i.e., 0.8 to 1 L), since the heat transfer rate at the entry region is higher between flowing fluid and the pipe wall. However, a high conducting metallic foam is attached exactly at the center of the pipe which is also trying to absorb more amount of heat from the wall and then it instantly transfers the heat to the fluid which tends to decrease the wall temperature at the foam attached region (i.e., 0.2 L to 0.8 L) compared to non-foam region of the pipe (i.e., 0 to 0.2 L and 0.8 to 1 L), as clearly seen in Fig. 6. It is observed from the comparison that the trend of the temperature profile obtained in the current study follows the trend of the experimental data of Baragh et al. [10]. In case of the experimental result obtained by Baragh et al. [10], wire mesh of 17 wires per inch was placed at different locations along the pipe length while in the current investigation metallic foam of 30 PPI having a length of 0.6 m along the pipe length is considered. The foremost reason to adopt metal foams instead of wire mesh in the current study is because of well-established fluid flow and heat dissipation models of metal foam reported in the literature. Due to insufficient literature and no firm establishment of heat dissipation models in the case of wire mesh, the present work uses metal foams for the heat enhancement study. As a result, the variation in the temperature profile has been noticed between the numerical and experimental results; but, the deviation of wall temperature amongst different porosities of 30PPI metal foam for different locations is found to be less.
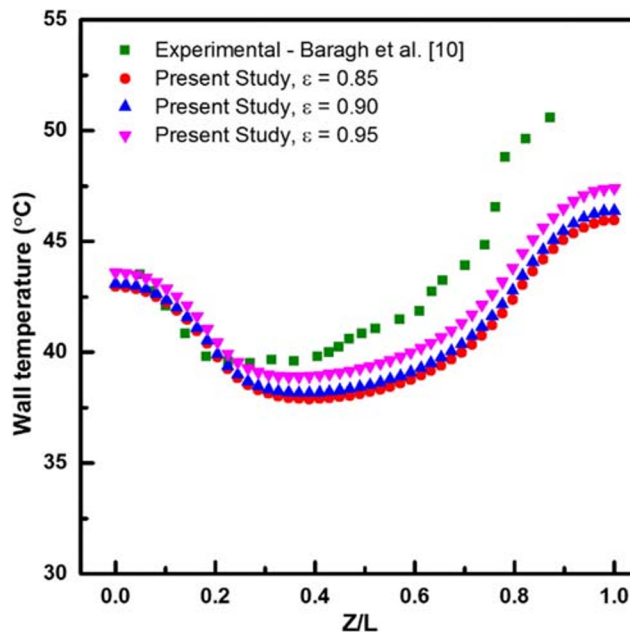
7 Results and discussion

7.1 Effect of pore density on wall temperature

The variation of wall temperature in the pipe for pore densities of 10, 20, 30 and 40 with a constant porosity of 0.90 copper metallic foam and for various flow regimes is shown in Fig. 7a–c. From the results, it is understood that the wall temperature declines with the increase in the PPIs of the copper metallic foam for all the flow features considered in the study. For example, the 40 PPI metal foam shows average decrease of 25.78%, 12.84% and 9.23% in wall temperature than 10 PPI metal foam in the laminar, transition and turbulent flow regimes, respectively. It is also noticed that the temperature on the wall of the pipe reduces at the metal foam attached region compared to non-porous region of the pipe for each PPI of the metallic foam. This is because the metal foam absorbs more heat from the pipe wall since it is directly attached to the wall and hence conduction plays significant contribution for dissipation of heat.

The wall temperature at the entry region of pipe is lower compared to the exit region since the heat transfer rate is higher at the entry between flowing fluid and the pipe wall. It is also clear from the results that, for a particular metallic foam pore density, the wall temperature decreases as flow Reynolds number increases. For example, the pore density of 10 shows a mean decrease of 21.89% and 31.84% in wall temperature for transition and turbulent flows, respectively compared to laminar flow.

Fig. 7 Variation of pipe wall temperature for various pore densities of metal foam at **a.** $Re =$ 1125, **b.** $Re = 3500$ and **c.** $Re =$ 6437
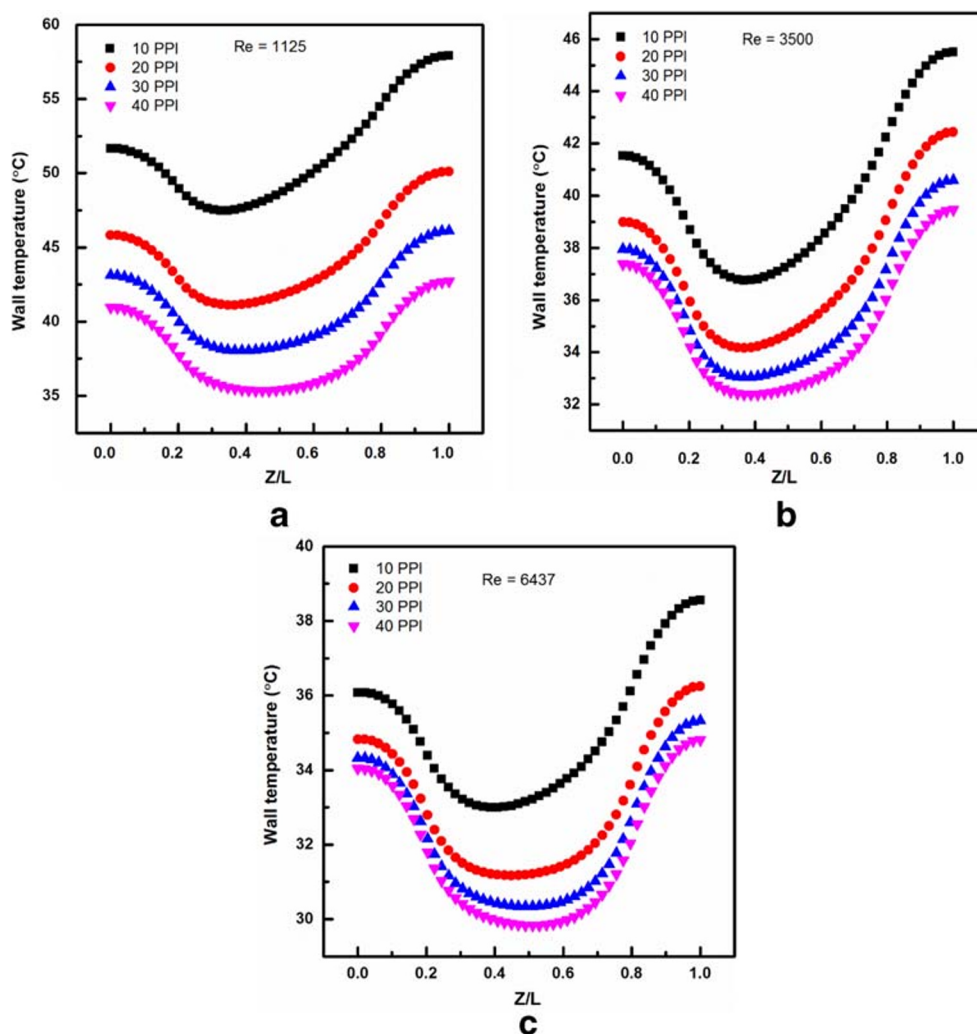
7.2 Wall temperature results of various metal foams

The variation of wall temperature of the pipe for the pore density of 40 with a constant porosity of 0.95 for copper, aluminium and nickel metallic foams for various flow regimes is shown in Fig. 8a–c. It is noticed from the plots that the decrement in wall temperature is found to be higher in the case of copper metal foam than aluminium and nickel metal foams for all the flow regimes studied. From Fig. 8d, it is explored that the average wall temperature declines with increasing flow Reynolds number for 40 PPI with a porosity of 0.95 for copper, aluminium and nickel metal foams. The decrement in the average wall temperature for copper metal foam is only 2.86%, 3.08% and 2.85% compared to nickel metal foam for laminar ($Re = 1125$), transition ($Re = 3500$) and turbulent ($Re = 6437$) flow regimes, respectively. The values of average wall temperature of aluminium metal foam are found between the copper and nickel metallic foams but very close to copper metal foam. It is also seen that the reduction in average temperature on the wall of the pipe for copper foam

is found to be 10.6% and 18.97% for transition and turbulent flows respectively compared to laminar flow and similar kind of results are observed for aluminium and nickel foams.

7.3 Results of Nusselt number (Nu)

The local Nu is computed based on D_h the pipe and it is defined in Eq. (17)

$$Nu_i = \frac{h_i D_h}{\lambda_{eff}} \tag{17}$$

where, Nu_i represents local Nusselt number of each set of data points, h_i represents local convection heat transfer coefficient of each data set (W/m²°C), D_h represents hydraulic diameter (m) and λ_{eff} represents effective conductivity of metallic foam (W/m°C) which is evaluated using relation given by Shokouhmand et al. [57].

$$\lambda_{eff} = \lambda_s^{(1-\varepsilon)} \lambda_f^{\varepsilon} \tag{18}$$

Fig. 8 Variation of wall temperature of the pipe for the metal foams **a.** $Re = 1125$, **b.** $Re = 3500$, **c.** $Re = 6437$ and **d.** average wall temperature
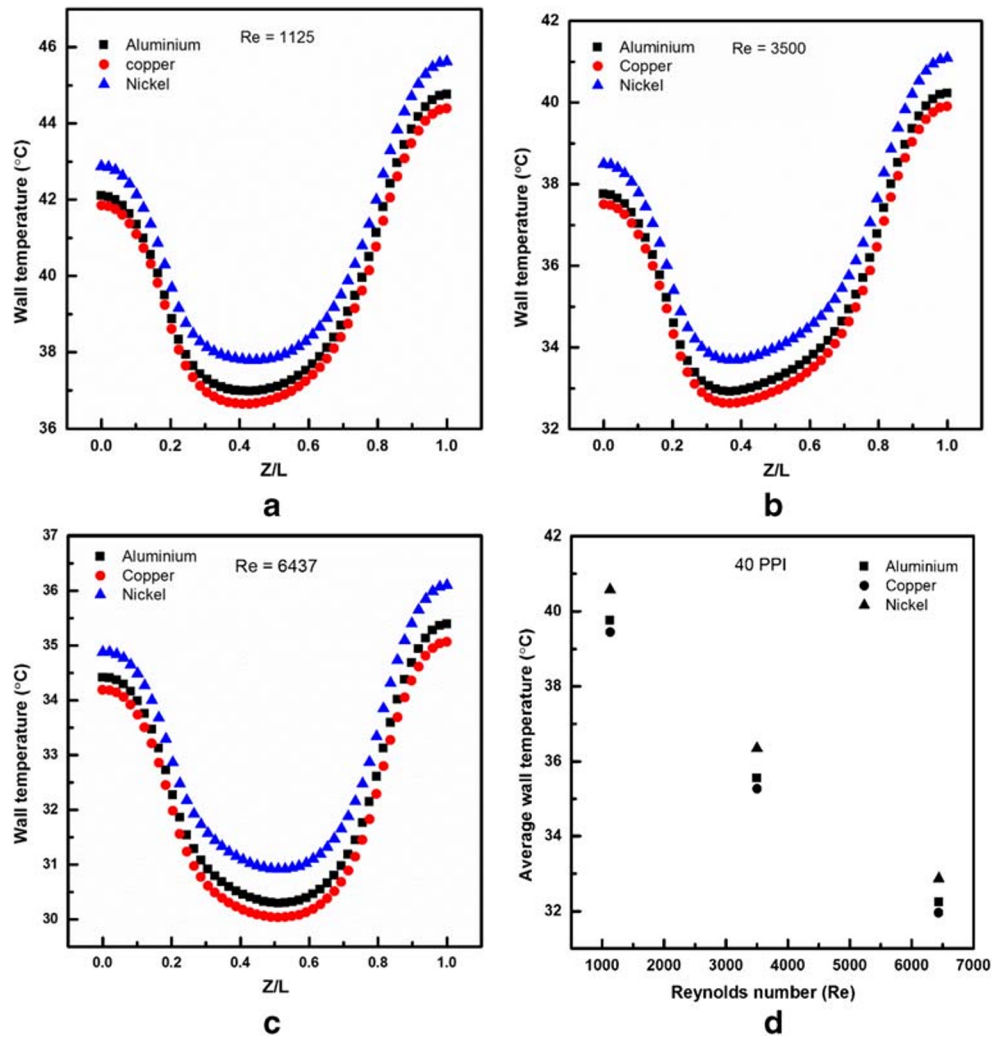
The local convection coefficient is evaluated based on Eq. (19)

$$h_i = \frac{q_w}{T_{w_i} - T_{f_i}} \tag{19}$$

where, q_w represents continuous heat flux boundary condition assigned on the wall in W/m^2, T_{w_i} represents wall temperature of each locations of data points in °C and T_{f_i} represents fluid temperature of each set data points in °C.

The average convective coefficient is evaluated based on Eq. (20)

$$\overline{h} = \frac{\sum_1^N h_i}{N} \tag{20}$$

where, $\overline{h}$ represents mean heat transfer coefficient in W/m^2°C, N represents total number of samples or each data points of calculated local convection coefficient.

The hydraulic diameter of the pipe is calculated using Eq. (21)

$$D_h = \frac{4A_c}{p} \tag{21}$$

where, A_c represents area of the pipe (m^2) and p denotes perimeter of pipe (m).

The mean surface Nusselt number is computed by Eq. (22)

$$\overline{Nu} = \frac{\overline{h}D_h}{\lambda_{eff}} \tag{22}$$

The Re computed based on D_h of pipe which is defined as

$$Re = \frac{\rho u D_h}{\mu_f} \tag{23}$$

where, ρ denotes fluid density (kg/m^3), u denotes fluid inlet velocity (m/s) and μ_f denotes viscosity of fluid (Ns/m^2).

The variations in local Nusselt number for metal foams through the pipe wall for various flow regimes are shown in Fig. 9a–d. Figure 9a–c detail the variation in local *Nu* for copper, aluminium and nickel metal foams for pore density of 40 with porosity of 0.95 for three different flow regimes considered in the present study. From the results it is observed that the improvement in local surface *Nu* is higher for copper metallic foam related to aluminium and nickel metallic foams for laminar (*Re* = 1125), transition (*Re* = 3500) and turbulent (*Re* = 6437) flow regimes respectively.

Initially, as the fluid enters the non-foam region of the pipe the difference in temperature between the wall and fluid is more; as a result, the heat carrying capacity of the fluid is more between 0 to 0.2 L region of the pipe. Further, the heat absorption

rate from the wall increases from 0.2 to 0.8 L due to high conducting metallic foam, which is attached at the center of the pipe. This leads to increase in Nusselt number for all the metallic foams. By the time fluid reaches 0.8 L, due to laminar flow condition heat transfer that takes place between the heated wall and the fluid decreases; later, between 0.8 L and 1 L there is no metal foam to assist heat transfer. But, in case of high Reynolds number 3500 and 6437, the flow is assisted by intense mixing of the fluid and the fluid is now forced to flow through the pores thereby an increase in the Nusselt number is observed compared to the Reynolds number 1125. For this reason, the Nusselt number is observed to be symmetry for Reynolds number 3500 and 6437 and non-symmetry for the Reynolds number 1125. These are clearly depicted in Fig. 9a–c.
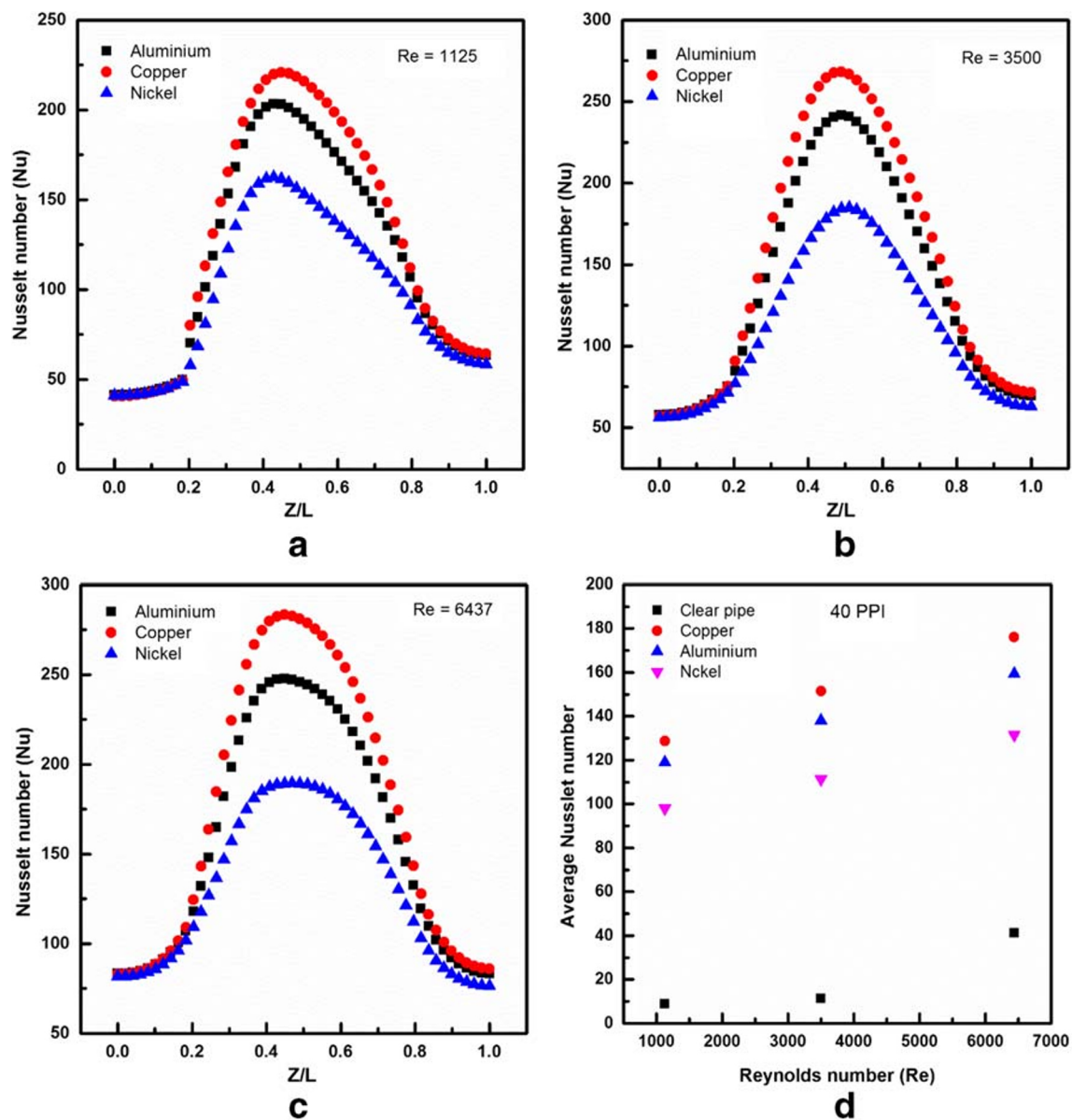
Fig. 9 Changes in local surface Nu for copper, aluminum and nickel metal foams **a.** *Re* = 1125, **b.** *Re* = 3500, **c.** *Re* = 6437 and **d.** average Nusselt number for 40PPI

Figure [9d](9d) demonstrates the variation in average Nusselt number for clear pipe and different metallic foams of 40 PPI with a porosity of 0.95 for varying Re. From the results it is noticed that the mean surface Nu increases with increasing Re for copper, aluminium and nickel metallic foams. It is also seen that the increase in average Nu is obtained high for copper metal foam because of its high effective conductivity. The copper metallic foam gives 17.72% and 36.86% increase in average Nusselt number at $Re = 3500$ and 6437 than $Re = 1125$. Also, the increment in average wall Nusselt number for copper metal foam is found to be 31.24%, 36.2%, 33.85% and 8.15%, 9.75%, 10.44% compared to nickel and aluminium metal foams at $Re = 1125$, $Re = 3500$ and $Re = 6437$ respectively. If one chooses aluminum metal foam insert in the pipe, the maximum deviation in average wall Nusselt number is found to be only10.44%.

7.4 Heat transfer enhancement ratio (Nu_ER)

The effectiveness of heat exchanger is computed from Nu_{ER} and is defined as the ratio of mean Nu for fully filled foam to the mean Nu for the clear pipe.

$$Nu_{ER} = \frac{\overline{Nu}}{\overline{Nu_\Phi}} \tag{24}$$

where, Nu_{ER} is referred as heat transfer enhancement ratio, $\overline{Nu}$ represents mean Nusselt number for filled foam in pipe and $\overline{Nu_\Phi}$ represents mean Nusselt number of empty pipe.

The heat transfer enhancement ratio is computed using Eq. [(24)](24) and is given in Fig. [10](10). Figure [10a](10a) explored the Nu_{ER} for copper metallic foam of various PPIs possessing porosity of 0.90 at Re = 1125, 3500 and 6437. The Nu_{ER} advanced with increasing pore densities of the metallic foam. This is due to increase in the superficial area density with increasing pore densities of the metallic foam. It is also observed that Nu_{ER} is higher at low flow rates compared to high flow rates of fluid. For 40PPI metal foam at $Re = 1125$, the Nu_{ER} increases by 111.27%, 40.5%, and 13.76% compared to pore density of 10, 20 and 30 respectively. Also, the average heat transfer enhancement ratio increases by 94.5% for 40 PPI related to 10 PPI copper metallic foam between the ranges of flow Reynolds number of 1125 to 6437.

The variations of Nu_{ER} for pore density of 20 with varying porosities of copper metal foams at three distinct Reynolds number are shown in Fig. [10b](10b). Figure [10b](10b) explored that the Nu_{ER} improves with increasing porosity of the metal foam. It is also seen that the Nu_{ER} is more at lower Re compared to higher Re. The heat transfer enhancement ratio increase by 137.66% and 50.53% for porosity 0.95 compared to porosities 0.85 and 0.90 respectively at $Re = 1125$. It is also noticed that Nu_{ER} for porosity 0.95 metal foam increases by 137.66%,

137.3% and 136.92% compared to 0.85 porosity at $Re = 1125$, 3500 and 6437 respectively.

The results of heat transfer enhancement for 40 PPI with porosity 0.95 for copper, aluminium and nickel metal foams are compared for different flow regimes ($Re = 1125$, 3500 and 6437) and are shown in Fig. [10c](10c). From the results, it observed that Nu_{ER} is obtained to be high for copper metal foam compared to aluminium and nickel metallic foams for all the flow rates. The average heat transfer enhancement ratio increases by 9.42% and 33.67% for copper foam compared to aluminium and nickel metallic foams between the ranges of Reynolds number of 1125 to 6437.

7.5 Colburn *j* factor and performance factor

To design any heat exchanging device, the thermal performance is an important parameter which can be computed using Colburn j factor and is given by the relation as:

$$\text{Colburn } j \text{ factor}, \quad j = \text{St.Pr}^{\frac{2}{3}} \tag{25}$$

where, St denotes Stanton number and Pr denotes Prandtl number.

Figure [11a](11a) demonstrates the changes of Colburn j factor for different PPI of copper metallic foam with Re considered in the present study. Figure [11a](11a) explored the Colburn j factor diminutions for all PPI of the metallic foam with corresponding Re of fluid considered in the study. It is also seen that 40 PPI metal foam shows the highest Colburn j factor for lower flow rates; however, there is no much deviation for 20 and 30 PPI metallic foam at higher flow rates. The pore density of 10 metallic foam shows the least Colburn j factor related to other PPI of metallic foams, which implies that the 10 PPI metallic foam gives the least thermal performance. Similar kind of results is observed for the porous medium reported in the literature [58]. The 40 PPI metal foam gives 111.56% and 65.62% higher Colburn j factor compared to 10 PPI metal foam at Reynolds number equal to 1125 and 8500 respectively.

Figure [11b](11b) explored the comparative study of Colburn j factor for 40 PPI of copper, aluminium and nickel metallic foams with respect to flow rates treated in current study. The Colburn j factor is 15.8% and 18.74% higher for copper metallic foam related to nickel metallic foam at flow Re of 1125 and 8500 respectively and the performance of aluminium metal foam is found in between them. This is because of the copper metallic foam attains high convective coefficient which is proportional to the St. However, the Colburn j factor declines with corresponding flow rates of the fluid for copper, aluminum and nickel metallic foams.

The overall thermal performance of metallic foam can be examined using the dimensionless parameter called the performance factor and is defined as the ratio of Colburn j factor
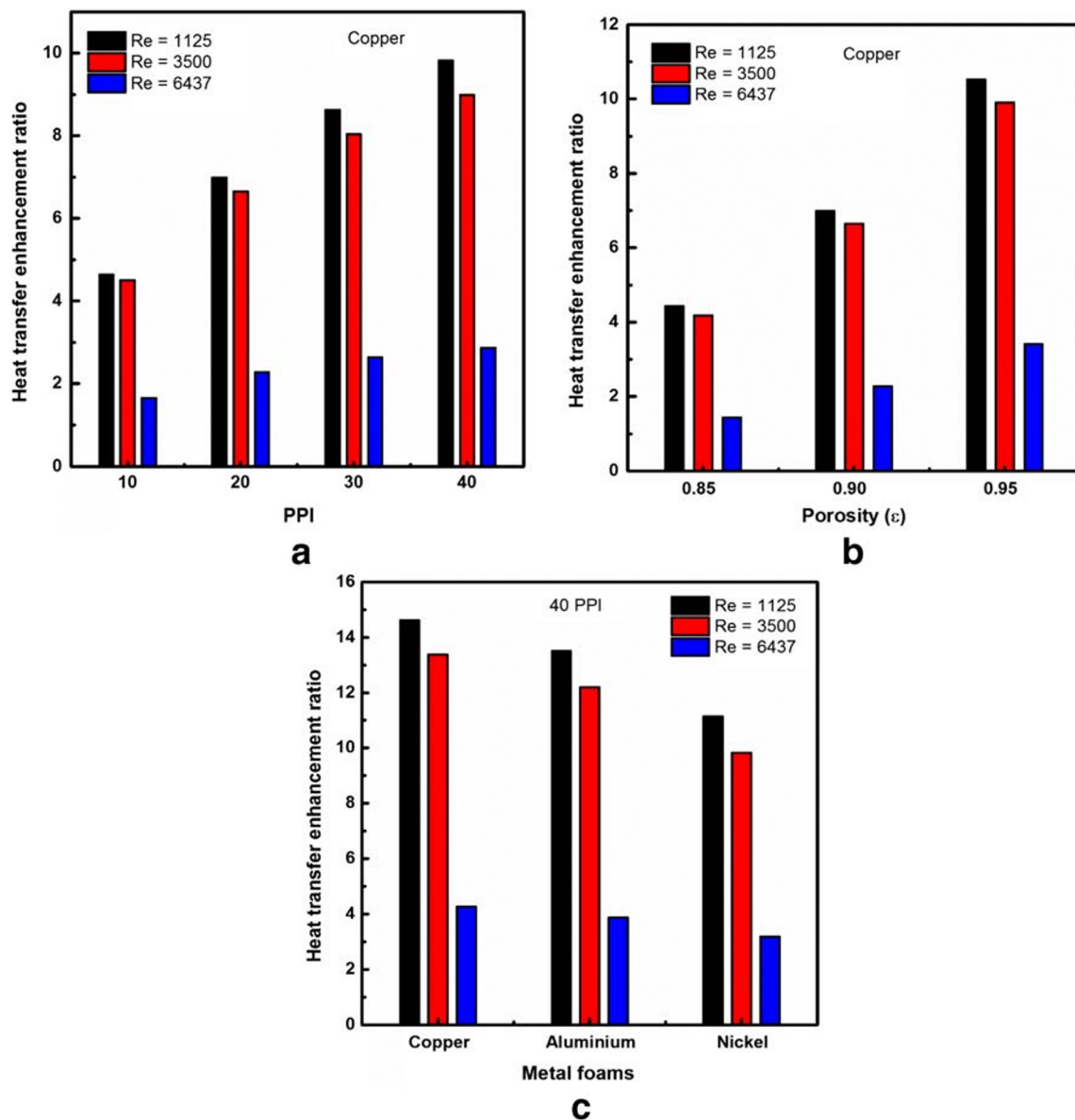
Fig. 10 Variation of Nu_{ER} for **a.** effect of pore densities, **b.** effect of porosities of metal foam and **c.** comparative study of copper, aluminum and nickel metal foams

to the pumping power of the fluid and is given by Manglik [59].

$$\text{Performance factor,} \quad \eta_p = \frac{\text{St Pr}^{\frac{2}{3}}}{f^{\frac{1}{3}}} \quad (26)$$

Figure 12a demonstrates the thermal performance factor for 10, 20, 30 and 40 PPI copper metallic foam with respect to Re. Figure 12a explored that the performance factor reduces with increasing Re. The 40 PPI metallic foam shows the highest performance factor for lower flow rates and goes on reducing with higher flow rates. The performance factor for 40 PPI metallic foam is 99.23% and 65.5% higher related to 10 PPI metallic foam at Re of 1125 and 8500 respectively.

The performance factor for distinct materials of metallic foam for pore density of 40 with respect to flow rates is revealed in Fig. 12b. It is noticed that the copper metallic foam gives higher performance factor by 4.65%, 15.8% and 6.2%, 19.1% compared to aluminium and nickel metallic foams respectively at $Re = 1125$ and 8500. The copper metallic foam attains higher heat transfer coefficient than the aluminium and nickel metallic foams which is directly proportional to the Stanton number with same pumping power.

7.6 Thermal entropy generation rate

Effect of pore densities Heat entropy generation for different Re for changes in pore density aluminium metallic foam
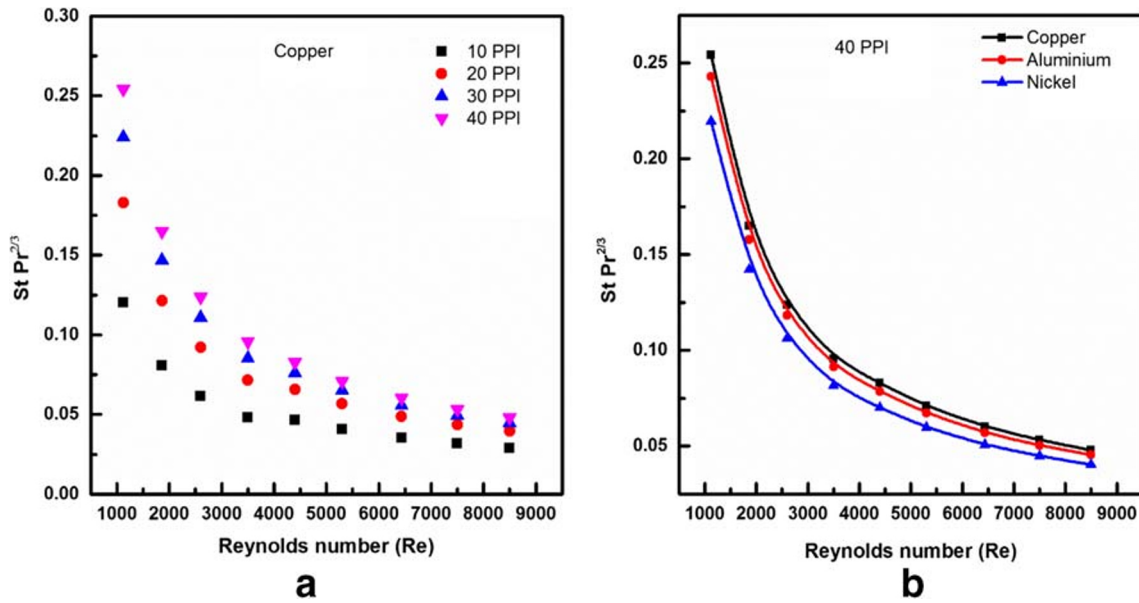
Fig. 11 Changes in *j* with corresponding *Re* for **a.** effect of PPI of the metallic foam, **b**. effect of distinct materials of metallic foam

having porosity of 0.90 is computed using Eq. (13) and is depicted in Fig. 13. Figure 13 explored that the thermal entropy generation rate drops with surge in PPIs of metal foam as well as with increasing *Re*. A significant decrease in heat entropy generation rate for 40 PPI metallic foam is observed than the 10 PPI metallic foam and only a marginal decrease is seen with 30 PPI metal foam. The thermal entropy generation rate decrease by 48.48% and 37.68% for 40 PPI aluminium metal foam compared to 10 PPI at *Re* = 1125 and 8500 respectively. This is because the specific surface area increases with increasing PPIs of the metal foam and hence it enhances more conduction than convection which results in decrease of wall temperature of the pipe. Hence, in order to minimize the irreversibility due to heat, the higher pore density metal foam is preferred.

Effect of porosities Figure 14 explored the heat entropy generation rate for 30 pore density aluminium metal foam for distinct porosities. From the results, it is seen that the thermal entropy generation rate reduces significantly with rise in porosity of the metal foam as well as with increasing flow *Re*. The porosity of 0.95 shows the least heat entropy generation compared to porosities of 0.85 and 0.90 for all Reynolds number. In addition, the heat entropy generation rate decreases by 33.31% and 51.54% for porosity of 0.90 and 0.95 compared to porosity of 0.85 at flow Reynolds number 8500.

Comparative study of distinct materials of metal foam From the above results, it is inferred that higher PPI and high porosity metal foam is best suitable for minimizing the thermal irreversibility of the system. In this account, the changes in thermal

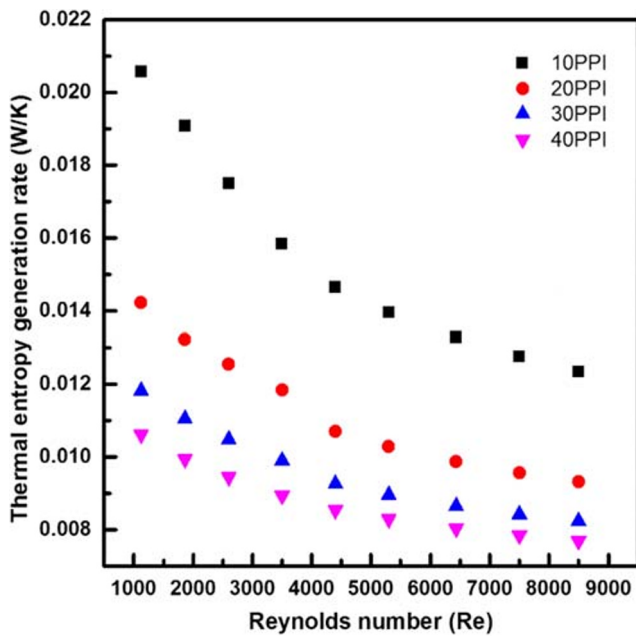**Fig. 12** Changes in η_p with *Re* for **a** effect of pore densities and **b** effect of distinct materials of metal foam
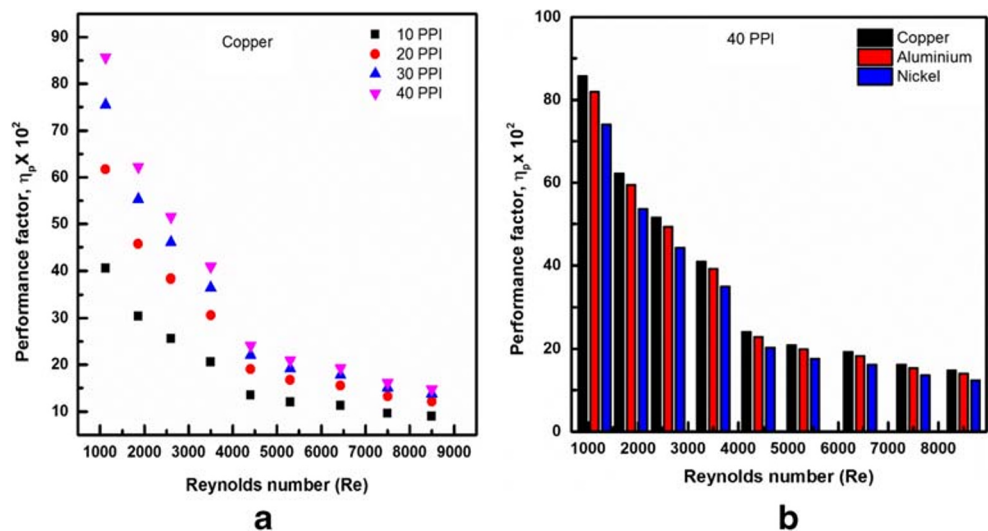
Fig. 13 Variation of heat entropy generation for changes pore densities of metal foam

Fig. 15 Changes in thermal entropy generation rate for various metallic foams

entropy generation rate for 40 PPI with porosity of 0.95 for aluminium, copper and nickel metal foams is compared and presented in Fig. 15. From the results it is seen that the heat entropy generation declines with increasing flow Reynolds number for different metallic foams. The copper metal foam shows significant reduction in heat entropy generation rate related to nickel metal foam and marginal reduction when compared to aluminium metallic foam. This is because of the reduction in wall temperature of nickel metallic foam which is lesser
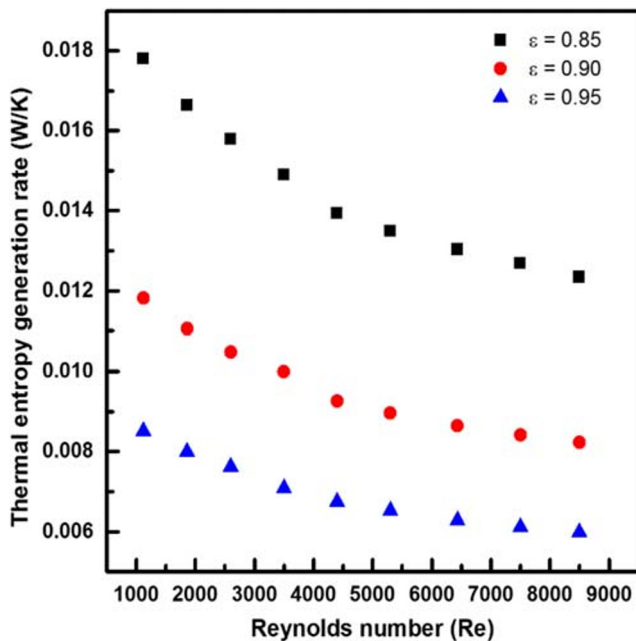
than the copper and aluminium metallic foams due to lesser effective conductivity. The heat entropy generation for copper metal foam decreases by 21.09% and 8.95% compared to nickel and aluminium metal foams at $Re = 8500$.

7.7 Frictional entropy generation rate

Effect of pore densities The changes in frictional entropy generation for aluminium metallic foam with porosity of 0.90 is revealed in Fig. 16. The frictional entropy generation is

Fig. 14 Changes in heat entropy generation rate for different Reynolds number
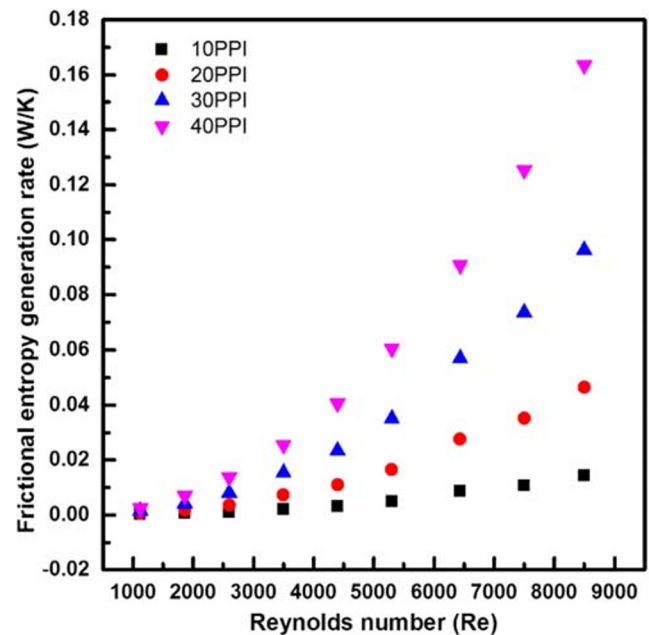

Fig. 16 Variation of frictional entropy generation rate for aluminum foam

computed using the Eq. (14). From the results, it is witnessed that the frictional entropy generation improves with increment in PPI of the metal foam as well as with flow rates. It is also seen that the frictional entropy generation is greater for 40 PPI compared to the other PPIs of aluminium metal foam. Because, increase in metallic foam PPI increases the specific surface area which in turn reduces the fluid flow through the porous metal foam and results in increased friction coefficient. On the other hand, the irreversibility due to friction is more or less similar for all PPI of the metallic foam at lower flow rates and increases significantly with increasing flow rates for all PPI of the metallic foam. The frictional entropy generation rate increase by 66.67% for 40 PPI related to 30 PPI aluminium metallic foam at $Re = 8500$.

Effect of porosities The changes in frictional entropy generation for 40 PPI aluminium metal foam with distinct porosities is evaluated by using Eq. (14) and is shown in Fig. 17. From the results it is witnessed that the frictional entropy generation rises with increasing Reynolds number. It is also seen that reduction in frictional entropy generation with varying porosities of the metal foam. The reason is that with the use of higher porosities of metallic foam, the pressure drop reduces and is proportional to the friction factor. Also, the surface area available to interact with the fluid is minimal. Additionally, the frictional entropy generation is found to be similar at low Re and progressively increases due to increase in flow Re. The frictional entropy generation decrease by 33.1% and 18.2% for porosity of 0.95 compared to porosity of 0.85 and 0.90 of aluminium metal foam at $Re = 8500$.
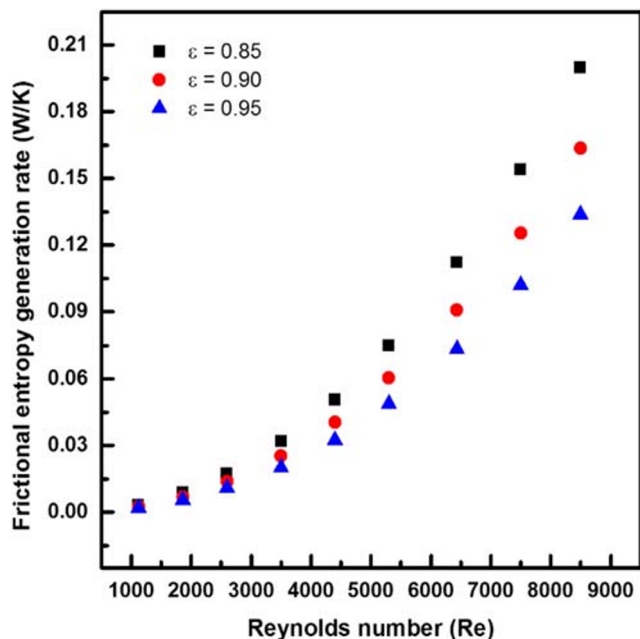
Comparative study for distinct materials of metal foams From the above results it is concluded that, lower PPI with high porosity of the metal foam is preferred because the irreversibility due to friction is minimum. Henceforth, the frictional irreversibility results are compared for aluminum, copper and nickel metal foam for 10 PPI with porosity of 0.95 is shown in Fig. 18. Figure 18 explored the frictional entropy generation shows similar results for all distinct metallic foams. The pressure drop is found to be same for aluminium, copper and nickel metallic foams with all flow rates. For equal pressure drop the copper and aluminium metal foam, enhance the higher heat dissipation with minimal entropy generation rate related to nickel metal foam.

7.8 Bejan number (Be) study

Effect of pore densities The Bejan number is computed using Eq. (16) and presented in Fig. 19. The variation of Bejan number for porosity of 0.95 with distinct pore densities of aluminium metallic foam is compiled in Fig. 19. From the results, it is witnessed that the Bejan number decreases with increment in pore densities of metal foam as well as with increase in flow rates. The 40 PPI aluminium metal foam shows significant decrease in Bejan number related to 10 PPI metallic foam with respect to the flow Reynolds number. Since, the frictional irreversibility is dominating over the thermal irreversibility with higher PPI metal foam. The minimal values of Bejan number are found to be 0.401, 0.1145, 0.07 and 0.04 for pore densities of 10, 20, 30 and 40 respectively at $Re = 8500$. Also the Bejan number decreases by 90.02% for 40 PPI related to 10 PPI metallic foam at $Re = 8500$.
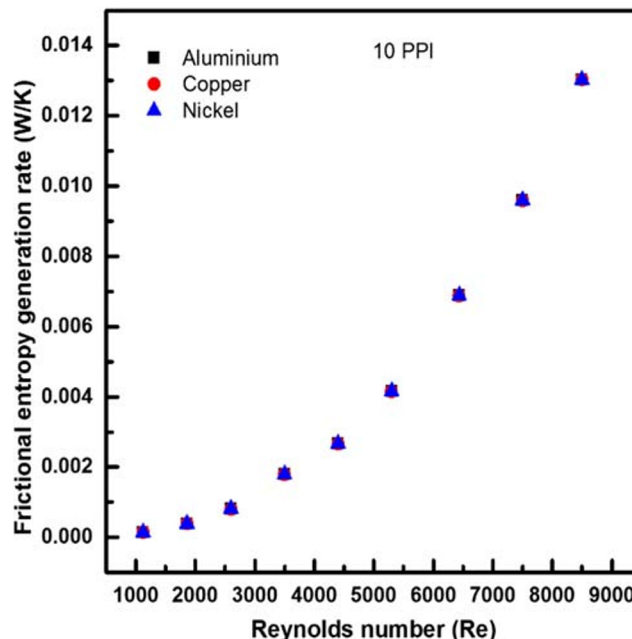

Fig. 17 Variation of frictional entropy generation rate for distinct porosities of metal foam
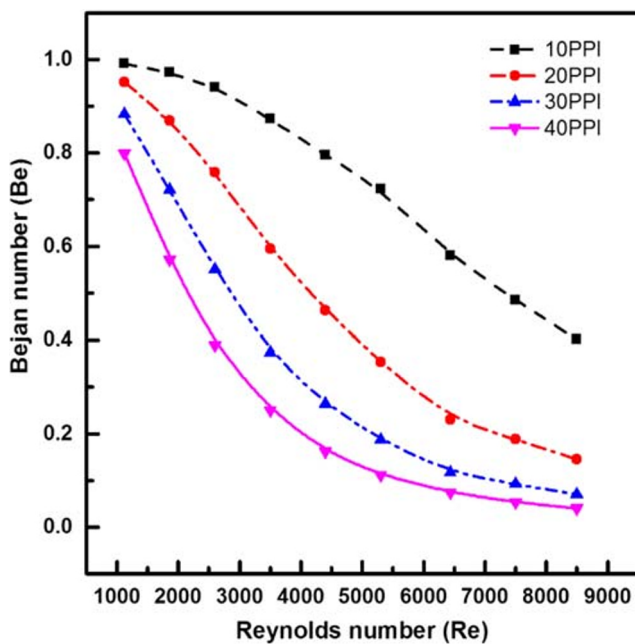

Fig. 18 Variation of frictional entropy generation rate for distinct materials of metal foam

Fig. 19 Changes in *Be* with *Re* for different PPI of metallic foam

Fig. 21 Changes in *Be* with *Re* for different conductivity of metallic foam

Effect of porosities The variation of Bejan number for 30 PPI with three distinct porosities of aluminium metallic foam is presented in Fig. 20. From the results it is explored that the Bejan number declines with increment in the porosities of the metal foam as well as increasing flow Reynolds number. It is also noticed that the porosity of 0.95 shows the least Bejan number and decreases marginally compared to the porosities of 0.85 and 0.90. The Bejan number decreases by 17.97% and 11.75% for porosity of 0.95 related to porosities of 0.85 and 0.90 for aluminium metal foam respectively at *Re* = 8500.
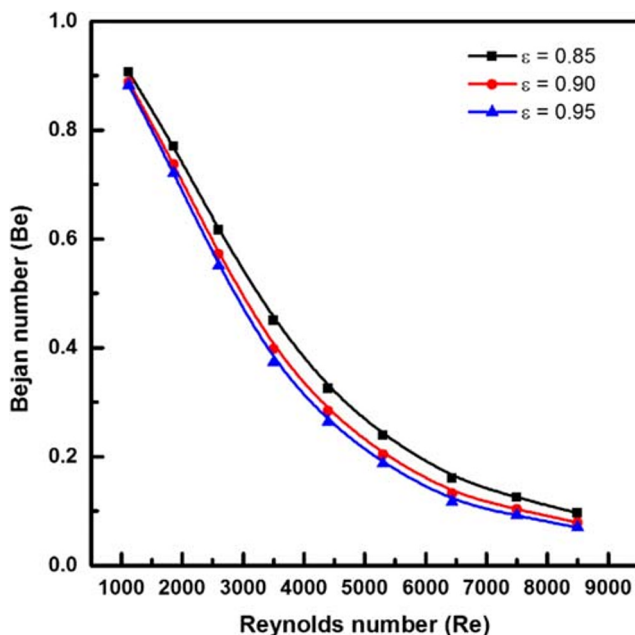
Comparative study of distinct materials of metallic foams From the above results it is concluded that the Bejan number is found to be lesser for higher PPI with high porosity of the metal foam. Therefore, the results of Bejan number are compared for aluminium, copper and nickel metallic foams. The variation of Bejan number for pore density of 40 with porosity of 0.95 for distinct metallic foam is depicted in Fig. 21. From the results it is observed that the *Be* decreases progressively with increasing flow rates of fluid. It is also noticed that the copper metal foam shows the least Bejan number compared to aluminium and nickel metallic foams. Since, the thermal irreversibility is significantly less for the copper metallic foam than the nickel metallic foam and marginally compared to aluminium metal foam. It also entails that frictional irreversibility is found to be same for aluminium, copper and nickel metallic foams because of the same pressure drop. From the comparison results of Bejan number for distinct materials of metallic foam, it is found that the heat irreversibility plays a crucial role than the frictional irreversibility.

8 Conclusions

Two-dimensional numerical computations of forced convection heat dissipation and entropy generation rate through copper, aluminium and nickel porous metallic foams filled in the horizontal cylindrical pipe were accomplished using ANSYS FLUENT. The horizontal pipe of 0.1 m diameter and 7 mm thick was filled with metallic foam of different pore density, porosities and made of different materials were considered for the numerical exploration. The features of fluid flow, heat

Fig. 20 Changes in *Be* with *Re* for different porosities of metallic foam

emission and the entropy generation are computed for distinct flow rates. Based on the present study, the salient features made on the study are as follows.

- On account of the decrease in average wall temperature for 40PPI with porosity of 0.95, the copper metal foam is only 2.86%, 3.08% and 2.85% compared to nickel metal foam for laminar transition and turbulent flow regimes, respectively; on the other hand, the average wall temperature of aluminium for the same PPI is found closer to copper metal foam.

- If one chooses the pore density of 40 aluminum metal foam insert in the pipe, the maximum deviation in average wall Nusselt number is found to be only 10.44% compared to copper metallic foam between for the Reynolds number ranging from 1125 to 6437.

- The heat transfer enhancement ratio for copper metallic foam increases marginally compared to aluminium metal foam and significantly compared to nickel metallic foam. The copper metallic foam increases the heat transfer enhancement ratio by 36.15% and 33.67% than nickel metal foam for transition and turbulent flow regimes. However, an increase of only 8.84% is found between copper and aluminum.

- The Colburn j factor and the performance factor decreases with increasing flow rates as well as increase in PPI of the metallic foams. The j and η_p for 30 and 40 PPI metallic foams shows similar kind of results beyond the Reynolds number of 4000. Hence, one can choose the 30 PPI metal foam instead of 40 PPI for similar performance factor of heat exchanging devices in order to minimize the pumping power.

- From the study, it confirms that the heat irreversibility can be minimized with the use of high porosity, high pore density and high conductivity of the metallic foams and in contrary, frictional irreversibility can be minimized with use of low pore density, high porosity with irrespective of the thermal conductivity of the metallic foams.

- The Bejan number decreases with increasing pore densities of the metallic foam as well as increasing porosities of the metal foam with increment in flow Reynolds number. It is also seen that the copper metal foam shows the least Bejan number compared to aluminium and nickel metal foam. It entails that the heat irreversibility is dominating over the frictional irreversibility.

References

1. Nazari M, Ashouri M, Kayhani MH, Tamayol A (2015) Experimental study of convective heat transfer of a nanofluid through a pipe filled with metal foam. Int J Therm Sci 88:33–39. https://doi.org/10.1016/j.ijthermalsci.2014.08.013

2. Xu HJ, Qu ZG, Lu TJ et al (2011) Thermal modeling of forced convection in a parallel-plate channel partially filled with metallic foams. J Heat Transf 133:092603. https://doi.org/10.1115/1.4004209

3. Xu HJ, Gong L, Zhao CY et al (2015) Analytical considerations of local thermal non-equilibrium conditions for thermal transport in metal foams. Int J Therm Sci 95:73–87. https://doi.org/10.1016/j.ijthermalsci.2015.04.007

4. Lin W, Xie G, Yuan J, Sundén B (2016) Comparison and analysis of heat transfer in aluminum foam using local thermal equilibrium or nonequilibrium model. Int J Heat Transf Eng 37:3-4, 314-322: 7632. https://doi.org/10.1080/01457632.2015.1052682

5. Lu W, Zhang T, Yang M (2016) Analytical solution of forced convective heat transfer in parallel-plate channel partially filled with metallic foams. Int J Heat Mass Transf 100:718–727. https://doi.org/10.1016/j.ijheatmasstransfer.2016.04.047

6. Celik H, Mobedi M, Oronzio Manca UO (2014) A pore scale analysis for determination of interfacial convective heat transfer coefficient for thin periodic porous media under mixed convection Int J Numer Methods Heat Fluid Flow. https://doi.org/10.1108/HFF-01-2017-0036

7. Kotresha B, Gnanasekaran N (2019) Effect of thickness and thermal conductivity of metal foams filled in a vertical channel – a numerical study. Int J Numer Methods Heat Fluid Flow 29:184–203. https://doi.org/10.1108/HFF-11-2017-0465

8. Gangapatnam P, Kurian R (2018) Numerical simulation of heat transfer in metal foams. Heat Mass Transf:553–562. https://doi.org/10.1007/s00231-017-2149-6

9. Li Z, Xia X, Li X, Sun C (2018) Discrete vs. continuum-scale simulation of coupled radiation and convection inside rectangular channel filled with metal foam. Int J Therm Sci 132:219–233. https://doi.org/10.1016/j.ijthermalsci.2018.06.010

10. Baragh S, Shokouhmand H, Ajarostaghi SSM, Nikian M (2018) An experimental investigation on forced convection heat transfer of single-phase flow in a channel with different arrangements of porous media. Int J Therm Sci 134:370–379. https://doi.org/10.1016/j.ijthermalsci.2018.04.030

11. Sheikhnejad Y, Hosseini R, Saffar Avval M (2017) Experimental study on heat transfer enhancement of laminar ferrofluid flow in horizontal tube partially filled porous media under fixed parallel magnet bars. J Magn Magn Mater 424:16–25. https://doi.org/10.1016/j.jmmm.2016.09.098

12. Bağcı Ö, Dukhan N (2018) Impact of pore density on oscillating liquid flow in metal foam. Exp Thermal Fluid Sci 97:246–253. https://doi.org/10.1016/j.expthermflusci.2018.04.020

13. Bamorovat Abadi G, Kim KC (2017) Experimental heat transfer and pressure drop in a metal-foam-filled tube heat exchanger. Exp Thermal Fluid Sci 82:42–49. https://doi.org/10.1016/j.expthermflusci.2016.10.031

14. Li Y, Wang S, Zhao Y (2018) Experimental study on heat transfer enhancement of gas tube partially filled with metal foam. Exp Thermal Fluid Sci 97:408–416. https://doi.org/10.1016/j.expthermflusci.2018.05.002

15. Nakayama CYKAA (2011) A local thermal non-equilibrium analysis of fully developed forced convective flow in a tube filled with a porous medium. https://doi.org/10.1007/s11242-011-9766-1

16. Yang C, Kuwahara F, Liu W, Nakayama A (2011) Thermal non-equilibrium forced convective flow in an annulus filled with a porous medium. The Open Transport Phenomena Journal 3:31–39

17. Lu X, Zhao Y (2019) International journal of heat and fluid flow effect of flow regime on convective heat transfer in porous copper manufactured by lost carbonate sintering. Int J Heat Fluid Flow 80:108482. https://doi.org/10.1016/j.ijheatfluidflow.2019.108482

18. Barlettta A, Magyari E, Pop I, Storesletten L (2008) Mixed convection with viscous dissipation in an inclined porous channel with

isoflux impermeable walls. Int J Heat Mass Transf 44:979–988. https://doi.org/10.1007/s00231-007-0324-x

19. Alomar OR (2019) Numerical investigation of two-phase flow in a horizontal porous evaporator with localised heating using non-Darcian flow and two equations model. Heat Mass Transf. https://doi.org/10.1007/s00231-019-02784-x

20. Tio K, Liu CY, Toh KC (2000) Thermal analysis of micro heat pipes using a porous-medium model. Heat Mass Transf 36:21–28

21. Edrisi S, Kasiri N, Maryam B (2017) A new approach to modeling the effective thermal conductivity of ceramics porous media using a generalized self - consistent method. Heat Mass Transf 53:321–330. https://doi.org/10.1007/s00231-016-1821-6

22. Jouybari NF, Maerefat M, Nimavari ME (2016) A pore scale study on turbulent combustion in porous media. Heat Mass Transf:269–280. https://doi.org/10.1007/s00231-015-1547-x

23. Ozdemir M, Ozguc AF (1997) Forced convective heat transfer in porous medium of wire screen meshes. Heat Mass Transf 33:129–136

24. Xu H, Zhao C, Vafai K (2017) Analytical study of flow and heat transfer in an annular porous medium subject to asymmetrical heat fluxes. Heat Mass Transf 53:2663–2676. https://doi.org/10.1007/s00231-017-2011-x

25. Bejan A (1979) Astudy of entropy generation in fundamental convective heat transfer. J Heat Transfer 101:718–725

26. Bejan A (1980) Second law analysis in heat transfer. Enegy 5(8):720–732

27. Bejan A (1982) Second law analysis in heat transfer and thermal design. Adv Heat Transfer 15:1–58

28. Bejan A (1996) Entropy generation minimization. CRC Press, New York

29. Nield DA (2006) A enote on a brinkman – brinkman forced convection problem, pp 185–188. https://doi.org/10.1007/s11242-005-2810-2

30. Nield DA (2007) The modeling of viscous dissipation in a saturated porous medium 129:1459–1463. https://doi.org/10.1115/1.2755069

31. Kurtbas I, Celik N, Dincer I (2010) Exergy transfer in a porous rectangular channel exergy transfer in a porous rectangular channel. Energy 35:451–460. https://doi.org/10.1016/j.energy.2009.10.011

32. Prommas R, Rattanadecho P, Cholaseuk D (2010) Energy and exergy analyses in drying process of porous media using hot air. Int Commun Heat Mass Transf 37:372–378. https://doi.org/10.1016/j.icheatmasstransfer.2009.12.006

33. Torabi M, Zhang K, Yang G et al (2015) Heat transfer and entropy generation analyses in a channel partially fi lled with porous media using local thermal non-equilibrium model. Energy 82:922–938. https://doi.org/10.1016/j.energy.2015.01.102

34. Torabi M, Dickson C, Karimi N (2016) Theoretical investigation of entropy generation and heat transfer by forced convection of copper – water nano fluid in a porous channel local thermal non-equilibrium and partial filling effects. Powder Technol 301:234–254. https://doi.org/10.1016/j.powtec.2016.06.017

35. Hunt G, Karimi N, Torabi M (2018) Two-dimensional analytical investigation of coupled heat and mass transfer and entropy generation in a porous , catalytic microreactor. Int J Heat Mass Transf 119:372–391. https://doi.org/10.1016/j.ijheatmasstransfer.2017.11.118

36. Hooman K, Haji-sheikh A (2007) Analysis of heat transfer and entropy generation for a thermally developing brinkman – brinkman forced convection problem in a rectangular duct with iso-flux walls. 50:4180–4194. https://doi.org/10.1016/j.ijheatmasstransfer.2007.02.036

37. Hooman K, Gurgenci H, Merrikh AA (2007) Heat transfer and entropy generation optimization of forced convection in porous-saturated ducts of rectangular cross-section 50:2051–2059. https://doi.org/10.1016/j.ijheatmasstransfer.2006.11.015

38. Srinivasacharya D, Bindu KH (2017) Entropy generation of micropolar fluid flow in an inclined porous pipe with convective boundary conditions. Sādhanā 42:729–740. https://doi.org/10.1007/s12046-017-0639-3

39. Bekir SZS, Yilbas S (2008) Entropy generation in flow field subjected to a porous block in a vertical channel. 179–197. https://doi.org/10.1007/s11242-007-9143-2

40. Tayari A, Ben A, Magherbi M (2015) Second law analysis in mixed convection through an inclined porous channel. Int J Thermophys 36:2881–2896. https://doi.org/10.1007/s10765-015-1925-0

41. Nazari M, Vahid DJ, Saray RK, Mahmoud Y (2017) Experimental investigation of heat transfer and second law analysis in a pebble bed channel with internal heat generation. Int J Heat Mass Transf 114:688–702. https://doi.org/10.1016/j.ijheatmasstransfer.2017.06.079

42. Oztop HF, Al-salem K (2012) A review on entropy generation in natural and mixed convection heat transfer for energy systems. Renew Sust Energ Rev 16:911–920. https://doi.org/10.1016/j.rser.2011.09.012

43. Ratts EB (2004) Entropy generation minimization of fully developed internal flow with constant heat flux 126:656–659. https://doi.org/10.1115/1.1777585

44. Khaboshan HN, Nazif HR (2019) Entropy generation analysis of convective turbulent flow in alternating elliptical axis tubes with different angles between pitches ; a numerical investigation. Heat Mass transf 55:2857–2872. https://doi.org/10.1007/s00231-019-02615-z

45. Pavel BI, Mohamad AA (2004) An experimental and numerical study on heat transfer enhancement for gas heat exchangers fitted with porous media 47:4939–4952. https://doi.org/10.1016/j.ijheatmasstransfer.2004.06.014

46. Sunden B (2012) Introduction to heat transfer. WIT Press, Ashurst, UK

47. Mahmoudi Y, Karimi N (2014) International journal of heat and mass transfer numericalinvestigation of heat transfer enhancement in a pipe partially filled with a porous material under local thermal non-equilibrium condition. Int J Heat Mass Transf 68:161–173. https://doi.org/10.1016/j.ijheatmasstransfer.2013.09.020

48. ANSYS Fluent (2017) ANSYSV R [ANSYS Fluent], 15.0, Help System, User's Guide/Theory Guide. ANSYS, Inc., Canonsburg, PA, http://www.ansys.com/Products/Fluids/ANSYS-Fluent

49. Walters DK (2019) A Three-Equation Eddy-Viscosity Model for Reynolds-Averaged Navier – Stokes Simulations of 130:. https://doi.org/10.1115/1.2979230

50. Kotresha B, Gnanasekaran N (2019) Numerical simulations of fluid flow and heat transfer through aluminum and copper metal foam heat exchanger – a comparative study numerical simulations of fluid flow and heat transfer through aluminum. Heat Transf Eng 0:1–13. https://doi.org/10.1080/01457632.2018.1546969

51. Huang ZF, Nakayama A, Yang K (2010) International journal of heat and mass transfer enhancing heat transfer in the core flow by using porous medium insert in a tube. Int J HeatMassTransf 53:1164–1174. https://doi.org/10.1016/j.ijheatmasstransfer.2009.10.038

52. Calmidi VV, Mahajan RL (2002) Forced convection in high porosity metal foams. J Heat Transf 122:557. https://doi.org/10.1115/1.128779

53. Zukauskas AA (1987) Convective heat transfer in cross-flow. In: Kakac S, Shah RK, Aung W (eds) Handbook of single-phase convective heat transfer. Wiley, New York

54. Singh PK, Anoop KB, Sundararajan T, Das SK (2010) International journal of heat and mass transfer entropy generation due to flow and heat transfer in nanofluids. Int J Heat Mass Transf 53:4757–4767. https://doi.org/10.1016/j.ijheatmasstransfer.2010.06.016

55. Ebrahimi A, Rikhtegar F, Sabaghan A, Roohi E (2016) Heat transfer and entropy generation in a microchannel with longitudinal

vortex generators using nano fluids. Energy 101:190–201. https://doi.org/10.1016/j.energy.2016.01.102

56. Garrity PT, Klausner JF (2015) Performance of aluminum and carbon foams for air side heat transfer augmentation 132:1–9. https://doi.org/10.1115/1.4002172

57. Shokouhmand H, Jam F, Salimpour MR (2011) The effect of porous insert position on the enhanced heat transfer in partially filled channels. Int Commun Heat Mass Transf 38:1162–1167. https://doi.org/10.1016/j.icheatmasstransfer.2011.04.027

58. Boomsma K, Poulikakos D, Zwick F (2003) Metal foams as compact high performance heat exchanger. Mech Mater 35(12):1161–1176

59. Manglik R M (2003) Heat transfer enhancement heat transfer handbook. Wiley Hoboken NJ, pp 1029–1130